

Internal resonance Raman scattering of characteristic target K x rays in thick silicon targets

James M. Hall, K. A. Jamison, O. L. Weaver, and Patrick Richard

Department of Physics, Kansas State University, Manhattan, Kansas 66506

T. Åberg

Laboratory of Physics, Helsinki University of Technology 02150 Espoo 15, Finland

(Received 28 September 1978; revised manuscript received 20 December 1978)

A four-inch curved-crystal spectrometer has been used to investigate the internal resonance Raman scattering (IRRS) process in Si K x-ray spectra induced by 1.5- and 2.0-MeV proton bombardment of thick targets. The IRRS process involves the scattering of characteristic target $K\alpha_{1,2}$ radiation off of the L shell of a neighboring target atom. The scattered photons exhibit an edge-shaped structure at ~ 1640.5 eV which tails off at low energies. A thick-target analysis has been used to obtain a partial scattering cross section for scattering within the observable energy range $1634 \leq E_f \leq 1640.5$ eV, which is in reasonable agreement with our calculations based on second-order perturbation theory. Based on the partial cross section, we are able to estimate the total IRRS cross section for scattering into all angles and all allowed energies ($0 \leq E_f \leq 1640.5$ eV) to be $(58 \pm 20)r_0^2$ or $(4.6 \pm 1.6)10^{-24}$ cm².

I. INTRODUCTION

In recent studies of the low-energy satellite structure of proton-induced silicon K x-ray spectra^{1,2} a small discontinuity was observed between the $KL_{23}L_{23}$ radiative Auger (RA) structure and the first radiative electron-rearrangement (KL^1 RER) peak. This discontinuity has an energy equal to the $K\alpha_{1,2}$ x-ray energy minus the $L_{2,3}$ binding energy and its spectral shape resembles an inverted K -absorption edge. Figure 1 displays a Si K x-ray spectrum obtained for 1.5-MeV H^+ on a thick Si target. The small edge-shaped peak labeled IRRS, at ~ 1640 eV is the structure of interest. Similar structures have been observed in photon-induced x-ray spectra of Si and S by Åberg and Utriainen.^{2,4} They attributed these structures to internal Raman scattering or characteristic $K\alpha$ x rays off of the L shell of neighboring Si atoms in the solid. We show in this paper that this process is dominated in Si by resonance scattering wherein a $K\alpha$ photon produced within a thick solid target by external photon or ion bombardment scatters off of a nearby ground-state Si atom producing a virtual intermediate state with a K -shell hole. In the transition to the final state this K -shell hole is filled by an L -shell electron and a photon with frequency ω_f is emitted. Since the ejected electron must undergo a "virtual free" to "free" transition in going to the final state, energy conservation requires that ω_f satisfy

$$\hbar\omega_i = \hbar\omega_f + I(2p) + \epsilon, \quad (1)$$

where $I(2p)$ represents the ionization energy of an $L_{2,3}$ electron, ϵ is the energy of the ejected electron, and in our experiment $\hbar\omega_i = \hbar\omega_{K\alpha}$. Since

the ejected electron and scattered photon are free to share available energy within the bounds of Eq. (1), then

$$\hbar\omega_f \leq \hbar\omega_{K\alpha} - I(2p), \quad (2)$$

where the equality holds for $\epsilon = 0$. This inequality gives rise to the high-energy cutoff in the IRRS structure that we observe.

The radiative Auger effect was first observed in the K x-ray spectra of Mg, Al, Si, and S by Åberg and Utriainen³ in 1969 and is described as a two-electron single-photon transition in which an outer-shell electron $n_f l_f$ transfers into an existing inner-shell hole $n_i l_i$ emitting a photon with frequency ω_f , and another outer-shell electron $n_f' l_f'$ is excited to a discrete or continuum state with energy ϵ . Most photons emitted in a radiative Auger transition have a continuous distribution of energies given by

$$\hbar\omega_f = I(n_i l_i) - I(n_f' l_f') - I(n_f l_f) - \epsilon, \quad (3)$$

where the I 's represent the appropriate ionization energies and, in particular, $I(n_f' l_f')$ represents the $n_f' l_f'$ ionization energy in the presence of $n_f l_f$ vacancy. The ejected electron and final photon share the available energy within the bounds of Eq. (3) so that

$$\hbar\omega_f \leq I(n_i l_i) - I(n_f l_f) - I(n_f' l_f'), \quad (4)$$

where the equality holds for $\epsilon = 0$. Thus the RA process also exhibits an edge-shaped structure with a high energy cutoff (Fig. 1). In the case of a $KL_{23}L_{23}$ radiative Auger transition Eq. (4) may be written

$$\hbar\omega_f \leq I(1s) - I(2p) - I(2p)' \leq \hbar\omega_{K\alpha} - I(2p)', \quad (5)$$

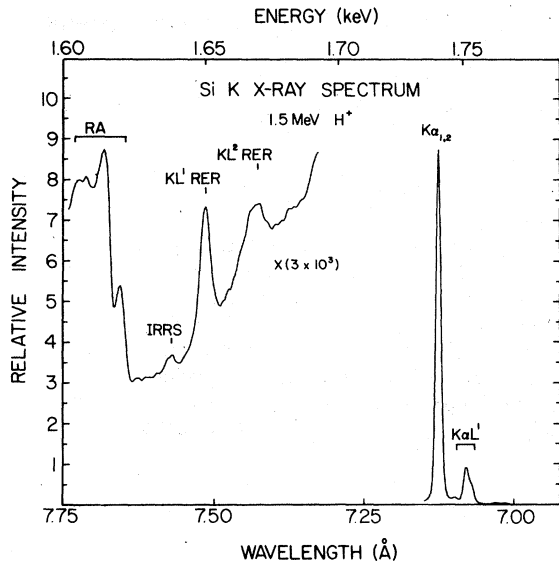


FIG. 1. Low-energy Si K x-ray spectrum containing the RA edge, the IRRS edge, and the KL^n RER structures in relation to the normal $K\alpha$ and first satellite lines.

where we do not distinguish between the L_2 and L_3 subshells. Comparing Eqs. (2) and (5) it is seen that the energy splitting between the RA and the IRRS cutoffs equals the difference between $I(2p)$ and $I(2p)^*$. The magnitude of this energy difference dictates whether or not it is possible experimentally to differentiate between processes that are internal to the atom (RA) and those that are external to the atom (IRRS).

Radiative electron rearrangement (RER), first described by Jamison *et al.*⁵ in 1975 is a third type of process that produces x rays below the $K\alpha_{1,2}$ energy. In the RER process a K x ray is emitted coincident with two $2s$ electrons undergoing a rearrangement. One of the $2s$ electrons fills a K -shell vacancy while the other is promoted to the $2p$ subshell. This process requires at least one $2p$ vacancy present in the atom in addition to a $1s$ vacancy. The lowest-energy RER is the transition from a state with one $1s$ and one $2p$ vacancy to a final state with two $2s$ vacancies (KL^1 RER in Fig. 1). The energy of the photon emitted in this transition is

$$\hbar\omega_f = \hbar\omega_{K\alpha} - [I(2s) - I(2p)] - [I(2s)^* - I(2p)^*], \quad (6)$$

where $I(2s)^*$ and $I(2p)^*$ are the ionization energies for states with a $2s$ and a $1s$ vacancy, respectively. The addition of an L -shell vacancy increases the energy of the RER transition creating an RER satellite, KL^2 RER in Fig. 1.

The energy systematics of the RA, IRRS, and

RER relative to $K\alpha_{1,2}$ are shown in Fig. 2. Silicon is the lowest Z element for which the IRRS process is observed in the region between the $KL_{2,3}L_{2,3}$ RA edge and the first RER satellite. The sulfur IRRS point on Fig. 2 was taken from photon induced x-ray spectra by Åberg and Utriainen.³ Internal Raman scattering has also been observed in photon-induced Ca and Ti K x-ray spectra by Sawada *et al.*⁶

Previous experimental work directed at studying the resonance Raman process has taken two approaches. Sparks,⁷ Bennett *et al.*,^{8,9} and Suortti¹⁰ have used monochromatic Cu $K\alpha$ or Mo $K\alpha$ x rays incident on Cr, Mn, Fe, Ni, Cu, Zn, Ge, and Ta targets to study the scattering cross section associated with the resonance Raman process while Eisenberger *et al.*^{11,12} have used synchrotron radiation incident on Cu metal to investigate the energy systematics of the process over an energy

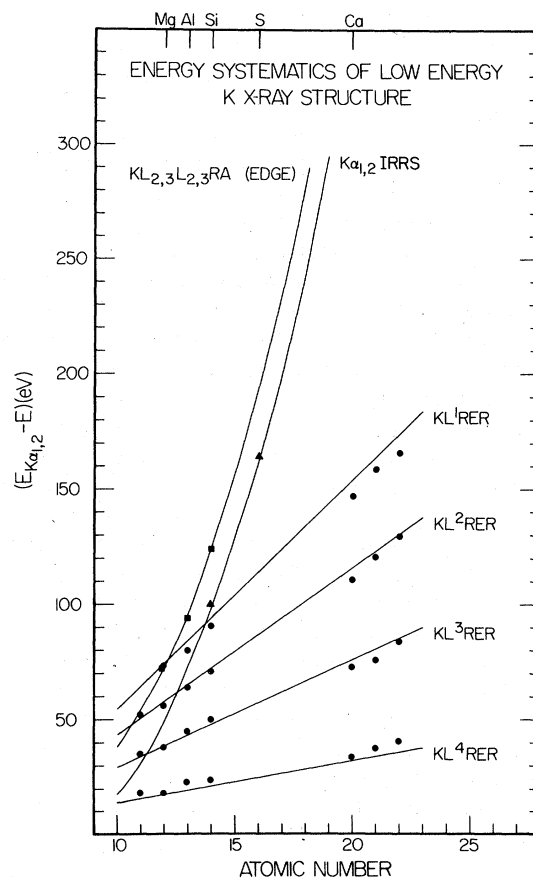


FIG. 2. Energy systematics of the low-energy Si K x-ray structures. Peak positions are plotted in terms of separation from the characteristic $K\alpha$ line. Solid lines are calculated energy separations. Experimental points are from Ref. 2, Jamison *et al.* (RER, RA); Ref. 3, Åberg *et al.* (S IRRS), and this work (Si IRRS).

range extending from the Cu K absorption edge to ~ 500 eV below it. Theoretical calculations of the scattering cross section for Cu $K\alpha$ radiation incident on Ni, Cu, Zn, and Ge have been made by Bannett and Freund¹³ and more recently by Tulkki and Åberg.¹⁴ Nozières and Abrahams¹⁵ have also discussed the x-ray resonance Raman scattering but with particular emphasis on the threshold singularities in metals. To our knowledge there has been no published work to date dealing specifically with the internal resonance Raman process as described here.

II. EXPERIMENT

The experiment consisted of bombarding a thick Si target with proton beams of 1.5 and 2.0 MeV. A 4-in. Applied Research Laboratories curved crystal vacuum spectrometer was positioned at 90° with respect to the beam axis. The Si target was positioned at 45° with respect to both the beam and spectrometer axis. Spectra were taken with the spectrometer Rowland circle perpendicular to the beam axis (\parallel mode) as well as coplanar with the beam axis (\perp mode). In the \parallel (\perp) mode the spectrometer is sensitive to radiation which is polarized parallel (perpendicular) to the beam axis. The intensity of the first RER peak was observed to decrease in going from the \parallel to \perp mode due to polarization effects.¹⁶ No polarization of the IRRS radiation was observed. Most of the data were taken in the \parallel mode. The spectrometer was fitted with 0.38-mm object and image (proportional counter) slits. The detector used was a flow mode proportional counter with a 2- μ m Makrofol window. The counter used a P10 gas flow (10% methane; 90% argon) and was operated at a negative bias of 2150 V.

Proton beams were produced by the Kansas State University single-stage AK-N Van de Graaff accelerator. Monoenergetic beams were momentum analyzed by a switching magnet and energy controlled by a fast-feedback slit control system. The beams were then focused by an electrostatic quadrupole and collimated to a 2-mm spot before striking the target. Typical beam currents in the range of 3–6 μ A were used to scan the x-ray region containing the RA, IRRS, and RER structures. A reduced beam current of ~ 150 nA was used to scan the x-ray region in the vicinity of the $K\alpha$ peak and its first satellite in order to obtain the ratio $K\alpha L^1/K\alpha_{1,2}$ required in the analysis as discussed in Sec. V. The reduced beam current was necessary in order to prevent pulse pileup and pulse-height defects in the proportional counter-preamplifier-amplifier system due to high count rates. The beam current was inte-

grated directly off the thick target and at each angular setting of the spectrometer crystal the x-ray intensity was accumulated for a preset number of microcoulombs of beam current. The data were accumulated in a Nuclear Data 100 analyzer with a multiscaling device allowing for a variable spectrometer step size and variable integrated current per spectrometer step. The data were punched on paper tape for later off-line analysis on a PDP-15 computer.

In order to ensure that the low-intensity Raman edge was not produced by geometrical effects due to the analyzing crystal, two different crystals were used to observe this effect. Si x-ray spectra obtained with ammonium dihydrogen phosphate (ADP) and ethylene diamine tartrate (EDdT) crystals both showed the Raman edge although the ADP spectra were lower in overall intensity. Most of the spectra in this experiment were taken with the EDdT crystal due to its higher reflectivity in the energy range of interest (~ 1600 – ~ 1660 eV). The spectrometer step size used with this crystal was 0.00067 Å. All spectra were obtained in first order (i.e., $n\lambda = \lambda = 2d \sin\theta$ for Bragg's Law).

III. THEORY

Various aspects of the theory of x-ray resonance Raman scattering have been discussed in the literature by several authors.^{7–16} In this section we outline this theory and apply it to IRRS. The Hamiltonian for a system of charged, spinless particles interacting with a radiation field in the nonrelativistic approximation may be written as the sum of three parts

$$H = H_R + H_{\text{atom}} + H_{\text{int}} \quad (7)$$

where H_R is the Hamiltonian for a free radiation field

$$H_R = \sum_{\alpha=\{\vec{k}, \lambda\}} a_{\alpha}^{\dagger} a_{\alpha} \hbar \omega_{\alpha},$$

H_{atom} is the Hamiltonian of an isolated atom

$$H_{\text{atom}} = \sum_j \frac{p_j^2}{2m_j} + \sum_{j \neq i} \sum_i \frac{1}{2} \frac{1}{4\pi\epsilon_0 r_{ij}},$$

and H_{int} is the interaction of the atom with the field

$$H_{\text{int}} = - \sum_j \frac{q_j}{m_j} \vec{A}(\vec{r}_j) \cdot \vec{p}_j + \sum_j \frac{q_j^2}{2m_j} A^2(\vec{r}_j).$$

H_{int} is broken into two parts, H_1 and H_2 , where H_1 is linear and H_2 is quadratic in \vec{A} . The index \vec{k} is the photon wave vector and λ is its polarization. The operator H_{int} may be treated as a perturbation that induces transitions between eigenstates of the unperturbed Hamiltonian

$H_R + H_{\text{atom}}$. Two photon processes can occur through second order transitions involving the $\vec{p} \cdot \vec{A}$ term in Eq. (7) or through first-order transitions involving the A^2 term.

The general transition rate for inelastic photon scattering including an ejected electron in the final state is given by Fermi's Golden Rule (neglecting any lifetime effects) taken to second order

$$d^4W_{if} = \frac{2\pi}{\hbar} \left| \langle F | H_2 | I \rangle + \sum_M \frac{\langle F | H_1 | M \rangle \langle M | H_1 | I \rangle}{E_I - E_M} \right|^2 \rho_\epsilon \rho_{\omega_f} d\epsilon d\Omega_\epsilon d(\hbar\omega_f) d\Omega_{\omega_f} \delta(E_F - E_I), \quad (8)$$

where ϵ is the energy of the ejected electron and the initial and final states are defined by

$$\begin{aligned} |I\rangle &= |i\rangle_{\text{atom}} \cdots n_{\alpha_i} \cdots n_{\alpha_f} \cdots \rangle_{\text{photons}}, \\ |F\rangle &= |f\rangle_{\text{atom}} \cdots (n_{\alpha_i} - 1) \cdots (n_{\alpha_f} + 1) \cdots \rangle_{\text{photons}} \end{aligned} \quad (9)$$

The first-order term $\langle F | H_2 | I \rangle$ does not involve intermediate states and is given by

$$\begin{aligned} \langle F | H_2 | I \rangle &= \frac{e^2 \hbar}{2\epsilon_0 m_e L^3} \frac{\vec{e}_{\lambda_i} \cdot \vec{e}_{\lambda_f}^*}{\sqrt{\omega_i \omega_f}} \\ &\times \sum_j \langle f | \exp[i(\vec{k}_i - \vec{k}_f) \cdot \vec{r}_j] | i \rangle \\ &\times \sqrt{n_{\lambda_i} (n_{\lambda_f} + 1)}, \end{aligned} \quad (10)$$

where n_{λ_i} (n_{λ_f}) represents the number of photons of polarization λ_i (λ_f) present in the initial (final) radiation fields and \vec{e}_{λ_i} (\vec{e}_{λ_f}) represents a unit polarization vector associated with the initial (scattered) photon. For the particular IRRS case considered in this paper, that of silicon $K\alpha$ radiation scattering off of δ a neighboring Si atom, $\hbar\omega_i = 1739$ eV and $0 \leq \hbar\omega_f \leq 1640$ eV so that $|(\vec{k}_i - \vec{k}_f) \cdot \vec{r}_j| \sim 0.03$. Thus the dipole approximation may be used and $\langle F | H_2 | I \rangle \sim 0$ for $|F\rangle \neq |I\rangle$. The second-order term in Eq. (8) describes those scattering processes in which an intermediate state is formed. The summation $\sum_M \cdots$ extends over all possible intermediate states M and may be expanded to yield

$$\begin{aligned} \sum_M \cdots &= \frac{e^2}{m_e^2} \left(\frac{\hbar}{2\epsilon_0 L^3} \right) \frac{\sqrt{n_{\lambda_i} (n_{\lambda_f} + 1)}}{\sqrt{\omega_i \omega_f}} \\ &\times \sum_m \left(\frac{\langle f | \vec{e}_{\lambda_f}^* \cdot \sum_j \vec{p}_j | m \rangle \langle m | \vec{e}_{\lambda_i} \cdot \sum_l \vec{p}_l | i \rangle}{E_i - E_m + \hbar\omega_i} \right. \\ &\quad \left. + \frac{\langle f | \vec{e}_{\lambda_i} \cdot \sum_j \vec{p}_j | m \rangle \langle m | \vec{e}_{\lambda_f}^* \cdot \sum_l \vec{p}_l | i \rangle}{E_i - E_m - \hbar\omega_f} \right), \end{aligned} \quad (11)$$

where E_i (E_m) is the energy of the atomic system in the initial (intermediate) state, j and l are electron labels and we have again made use of the dipole approximation. The first term on the right-hand side of Eq. (11) can be quite large if the in-

cident energy $\hbar\omega_i$ is close to some energy difference $E_m - E_i$ within the atom. This occurs, for example, if $\hbar\omega_i$ is near an atomic absorption edge as is the case in resonance Raman scattering.

The position and the shape of the observed IRRS feature imply that the final state contains a $2p$ hole and a low energy continuum electron. The only intermediate state with a low-energy continuum electron that is near resonance is the state $|1s^{-1}(\epsilon p)\rangle$. We neglect the effects of the M shell electrons of silicon and the possibility of flipping the spin of the ejected electron. Thus the atomic states to be considered are

$$\begin{aligned} |i\rangle &= {}^1S; (E_i), \\ |m\rangle &= (1s)^{-1}(\epsilon p)^1P; (E_m = E_i + \epsilon + \hbar\omega_K), \\ |f\rangle &= (2p)^{-1}(\epsilon p)^1S, {}^1P, {}^1D; (E_f = E_i + \epsilon + \hbar\omega_L), \end{aligned} \quad (12)$$

where $\hbar\omega_K$ ($\hbar\omega_L$) is the energy of an atomic K - (L -) shell hole and ϵ is taken to be the same in the intermediate and final states. Multiplet splitting of the final state has been ignored.

We neglect the second (nonresonant) term in Eq. (11), carry out the required sums over the L and m_L values of the intermediate and final states, and obtain after some algebra an expression for the differential cross section associated with spontaneous resonance Raman scattering

$$\begin{aligned} \frac{d^3\sigma_{\text{RR}}}{d\epsilon d\omega_f d\Omega_{\omega_f}} &= \frac{4r_0^2 \omega_f}{m_e^2 \hbar^2 \omega_i} \\ &\times \frac{|\langle 1s | p_x | 2p \rangle|^2 |\langle \epsilon p | p_x | 1s \rangle|^2}{(\omega_K + \omega - \omega_L)^2} \\ &\times \delta(\omega_i - \omega_f - \omega - \omega_L), \end{aligned} \quad (13)$$

where $\omega = \epsilon/\hbar$, r_0 is the classical electron radius, and Slater determinants have been substituted for the true atomic wave functions. The continuum electron wave function $\langle \epsilon p |$ has been normalized per unit energy interval. Equation (13) includes the integration over $d\Omega_\epsilon$, the solid angle associated with the ejected electron, and accounts for the two possible spin states of the ejected electron. Note also that it is independent

of the polarization vectors \vec{e}_{λ_i} and \vec{e}_{λ_f} . Hence it is readily applied to situations where the incident photon flux has zero net polarization and the final polarization is not measured.

We may relate the scattering cross section given by Eq. (13) to the K absorption cross section per atom (σ_K) by observing that

$$\sigma_K(\omega_K + \omega) = \frac{8\pi^2\alpha\hbar}{m^2(\omega_K + \omega)} |\langle \epsilon p | p_x | 1s \rangle|^2, \quad (14)$$

where α is the fine-structure constant. Integrating Eq. (13) over $d\Omega_{\omega_f}$ and $d\epsilon$ thus gives an expression for the energy differential cross section per atom associated with the resonant Raman scattering process

$$\frac{d\sigma_{RS}(\omega_f)}{d\omega_f} = \frac{2r_0^2}{\pi\alpha\hbar^2} \frac{\omega_f(\omega_{K\alpha} + \omega_i - \omega_f)}{\omega_i(\omega_{K\alpha} - \omega_f)^2} \times \sigma_K(\omega_{K\alpha} + \omega_i - \omega_f) |\langle 1s | p_x | 2p \rangle|^2. \quad (15)$$

By integrating this expression over ω_f , which varies from 0 to $\omega_i - \omega_L$, the total resonant contribution to the cross section is obtained. Recent work by Tulkki and Åberg¹⁴ has shown that inclusion of the second (nonresonant) term in Eq. (11) results in the addition of an anisotropic contribution to the scattering cross section $d^2\sigma_{RS}/d\Omega_{\omega_f}d\omega_f$. They estimate this contribution to be about 10% of the total cross section. Thus, for our purposes, we neglect the contribution of the nonresonant term. We also neglect any lifetime effects for the K hole state since the condition $(\omega_i - \omega_K)^2 \gg \Gamma_K^2/4\hbar^2$, where Γ_K is the linewidth associated with the K hole state is well

satisfied in our case. The calculated intensity profile of the scattering cross section for silicon $K\alpha$ radiation on solid silicon is shown in Fig. 3 for the energy range $1540 \leq E_f \leq 1645$ eV. The results of Eq. (15) have been convoluted with our instrument resolution function (a unit Gaussian with full-width at half-maximum equal to 2.5 eV) for comparison with our data.

IV. THICK TARGET ANALYSIS

In this section we outline the data analysis required in order to extract the IRRS and characteristic $K\alpha$ photon yields from a thick, homogeneous solid target. The details of the calculation are given in the appendix.

The $K\alpha$ photons involved in the IRRS process are produced as a result of K ionization produced by ion bombardment. The incident ions may be treated as a parallel, monoenergetic beam of arbitrary cross section and constant intensity up to the ion range (i.e., straggling is neglected). The total $K\alpha$ x-ray yield into some solid angle in the direction of a distant detector may be obtained from a thick target formula¹⁷ which accounts both for energy loss along the beam path (and thus for a variation in the K -vacancy production cross section with penetration depth) and for attenuation of the emitted photons along the exit path.

The total IRRS photon yield into the detector solid angle may be obtained by first calculating the rate at which $K\alpha$ photons are produced within a volume element dV' along the ion beam path. These photons are emitted isotropically from dV' and are attenuated [absorption coefficient

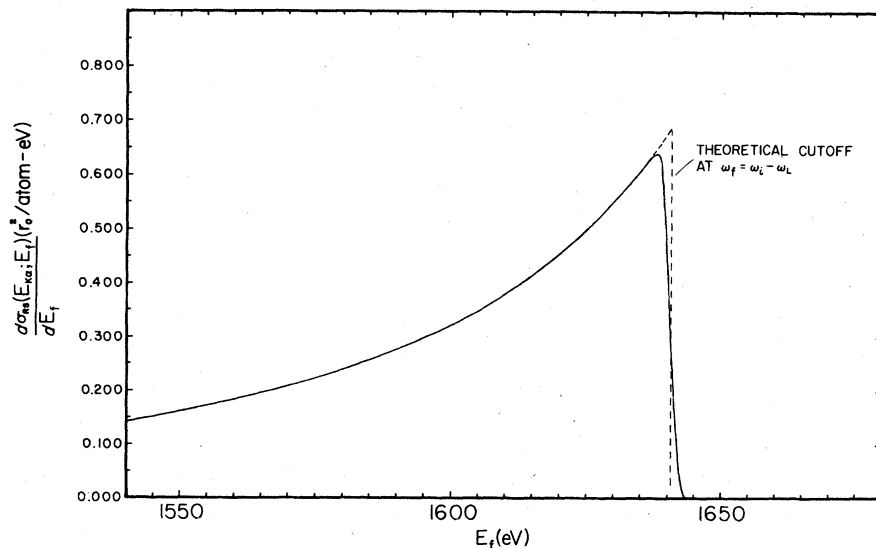


FIG. 3. Intensity profile for the IRRS process for Si $K\alpha$ radiation on Si calculated using Eq. (15) (dashed curve). The solid line is the profile convoluted with our instrument resolution function.

$\mu = \mu(E_{K\alpha})$] along a path to another volume element dV in which some fraction of them interact via the IRRS process. The rate of resonance Raman scattering within dV due to $K\alpha$ photons originating in dV' is proportional to the Raman scattering cross section $\sigma_{RS}(E_i, E_f)$. The scattered photons, which are assumed to have an isotropic angular distribution—see discussion following Eq. (15)—are then attenuated [$\mu = \mu(E_f)$] along the exit path to the detector. In calculating the total IRRS yield into a given detector solid angle one must integrate over contributions from all such elements dV for a fixed dV' and then over all elements dV' along the ion beam path.

The yield of the IRRS radiation in the vicinity of some energy E_f relative to the $K\alpha$ radiation for a given beam-target-detector orientation may be written in terms of σ_{RS} as

$$\frac{Y_{RS}(\alpha, \beta, E_f)}{Y_{K\alpha}(\alpha, \beta)} = \frac{\int d\omega_f (d\sigma_{RS}/d\omega_f)}{\sigma_{KX}(0)} \times F(\alpha, \beta, E_0, E_f), \quad (16)$$

where the integral represents a differential segment of σ_{RS} responsible for scattering incident radiation $E_{K\alpha}$ into the interval between E_f and $E_f + \Delta E_f$, $\sigma_{KX}(0)$ is the K x-ray production cross section at the incident ion energy E_0 , and $F(\alpha, \beta, E_0, E_f)$ is a dimensionless form factor that accounts for the scattering geometries, beam energy loss, and x-ray attenuation. α and β are angles that represent the beam-target and target-detector orientation respectively.

In the present experiment only a small energy segment of the IRRS spectrum near the high energy edge (see Figs. 1 and 3) is observed. Since the form factor $F(\alpha, \beta, E_0, E_f)$ is a slowly varying function of E_f in the immediate vicinity of the IRRS edge, we approximate $F(\alpha, \beta, E_0, E_f)$ by $F[\alpha, \beta, E_0, E_f(\max)]$ where $E_f(\max) = E_{K\alpha} - I(2p)$. $F[\alpha, \beta, E_0, E_f(\max)]$ may be computed by numerical means. The ratio of Y_{RS} to $Y_{K\alpha}$ may be determined experimentally and the result used to determine $\Delta\sigma_{RS} \equiv \int d\omega_f (d\sigma_{RS}/d\omega_f)$ integrated from the IRRS edge to an energy just below the edge.

V. DATA ANALYSIS

The x-ray spectra of Si bombarded with 1.5- and 2.0-MeV proton beams are shown in Fig. 4. The structure between 1630 and 1640 eV is attributed to the IRRS process with the ejected electron having very nearly zero energy and the photon having approximately the Si $K\alpha$ energy minus the $L_{2,3}$ ionization energy. The peak at 1650 eV has been identified² as the first tran-

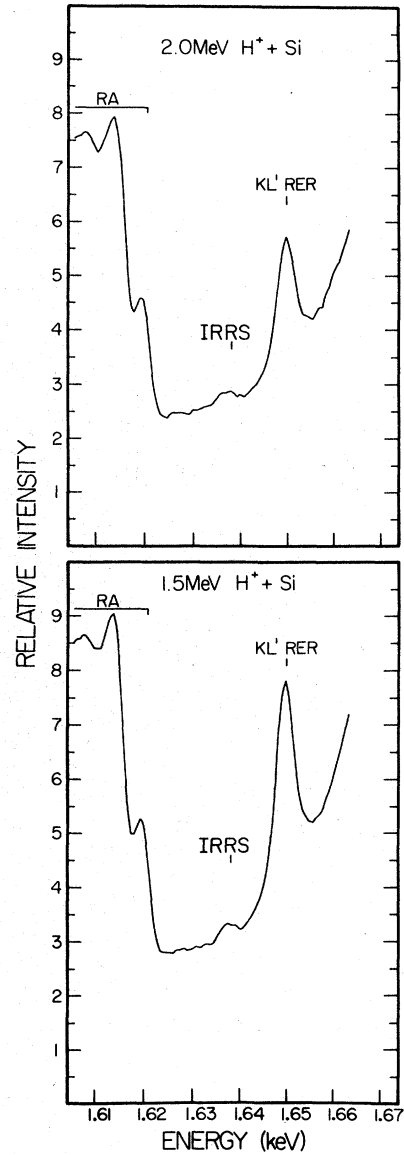


FIG. 4. K x-ray spectra of silicon for 1.5- and 2.0-MeV H^+ bombardment showing the RA, IRRS, and KL^1 RER intensities.

sition in the RER satellite sequence (KL^1 RER). The RER intensity is seen to decrease in going from 1.5 to 2.0 MeV. The RA edge structures are easily seen between 1600 and 1620 eV.

In Sec. III we established the spectral shape of the resonance Raman process to be approximately that of an inverted absorption edge tailing off at low energies. A comparison of Figs. 3 and 4 indicates that only a small portion (~ 6 eV) of the total width of this edge structure is actually visible amid the diverse background of our spectra. Thus without knowing the analytical

shape and background in the vicinity of the Raman edge, it becomes impossible from our data to directly measure the total cross section $\sigma_{RS}(E_i = E_{K\alpha})$ associated with the resonance Raman process. However, it is possible to measure directly a partial scattering cross section associated with scattering into an energy interval $1634 \leq E_f \leq 1640.5$ eV and from that partial cross section to estimate the total cross section $\sigma_{RS}(E_i = E_{K\alpha})$ for scattering into all angles and all allowed energies [$0 \leq E_f \leq E_f(\text{max})$].

The partial scattering cross section in the immediate vicinity of the Raman edge may be calculated using the results of Sec. IV (convoluted with our instrument resolution function) if the relative intensity $Y_{RS}/Y_{K\alpha_{1,2}}$ is known. The relative intensity can be determined from

$$\frac{Y_{RS}}{Y_{K\alpha_{1,2}}} = \frac{Y_{RS}}{Y_{KL}^1 \text{ RER}} \frac{Y_{KL}^1 \text{ RER}}{Y_{K\alpha L}^1} \frac{Y_{K\alpha L}^1}{Y_{K\alpha_{1,2}}}, \quad (17)$$

where $Y_{K\alpha L}^1$ and $Y_{KL}^1 \text{ RER}$ are the intensities of the first $K\alpha$ satellite line and the first RER line, respectively. Combining three separate relative intensity measurements results in a complicated experimental error analysis in $Y_{RS}/Y_{K\alpha_{1,2}}$; however, a direct measurement would involve a careful normalization between the IRRS and characteristic radiation portions of the spectra where the beam currents are radically different.

The ratios $Y_{RS}/Y_{KL}^1 \text{ RER}$ and $Y_{K\alpha L}^1/Y_{K\alpha_{1,2}}$ are measured in this experiment while $Y_{KL}^1 \text{ RER}/Y_{K\alpha L}^1$ has been measured previously by Jamison *et al.*² The measured values of the ratios are tabulated in Table I. Due to the low intensity and uncertain background in the IRRS region the intensity of the

Raman edge was taken to be the integrated intensity from the edge to 6.5 eV below the edge minus a trapezoidal background. The RER intensity was taken as the area of a Gaussian peak sitting on a background which was taken as a constant plus a Lorentzian tail due to the $K\alpha$ radiation. The intensities of the $K\alpha$ and first satellite ($K\alpha L^1$) lines were taken as the integrated intensities of each of the well resolved peaks.

Based on the data presented in Table I values for the relative intensity $Y_{RS}/Y_{K\alpha_{1,2}}$ of $(1.20 \pm 0.58) \times 10^{-5}$ for E_0 (incident proton energy) = 1.5 MeV and $(1.42 \pm 0.70) \times 10^{-5}$ for $E_0 = 2.0$ MeV are obtained. A slight rise in the relative intensity in going from 1.5 to 2.0 MeV is expected since the form factor in Eq. (16) also increases slightly over this range. The partial cross section for scattering into the energy interval $1634 \leq E_f \leq 1640.5$ eV may be obtained from Eq. (16). The results are $\Delta\sigma_{RS}(E_0 = 1.5 \text{ MeV}) = (4.2 \pm 2.0) r_0^2$ and $\Delta\sigma_{RS}(E_0 = 2.0 \text{ MeV}) = (4.6 \pm 2.3) r_0^2$. The cross section appears to be independent of the incident projectile energy within experimental uncertainty as expected.

An estimate for the resonance contribution to the partial scattering cross section can be obtained by convoluting the instrument resolution function with Eq. (14) and integrating over the region of interest ($1634 \leq E_f \leq 1640.5$ eV). This yields a value of $\Delta\sigma_{RS}(\text{theoretical}) = 3.88 r_0^2$ in reasonable agreement with our experiment. The total resonant contribution to the Raman scattering cross section is obtained by integrating over the entire range of E_f ($0 \leq E_f \leq 1640.5$ eV). This gives $\sigma_{RS}(\text{theoretical}) = 50.8 r_0^2$. In both calculations we have used Hartree-Fock single-electron wave functions in the numerical calculation of the matrix element $\langle 1s | p_x | 2p \rangle$ which was expressed in terms of the radial wave functions $R_{1s}(r)$ and $R_{2p}(r)$ as

$$|\langle 1s | p_x | 2p \rangle|^2 = \frac{1}{3} m_e^2 \omega_{K\alpha}^2 \left(\int_0^\infty R_{1s}(r) R_{2p}(r) r^3 dr \right)^2. \quad (18)$$

The $1s$ wave function was calculated in the presence of a $2p$ vacancy and the $2p$ wave function was calculated in the presence of a $1s$ vacancy. Values for the K absorption cross section $\sigma_K(\omega_{K\alpha} + \omega_i - \omega_f)$ were taken from the theoretical calculations of Scofield.¹⁸

The estimated partial scattering cross section amounts to 7.6% of the theoretical total scattering cross section. This gives an estimate for the total cross section of $\sigma_{RS}(\text{expt.}) = (58 \pm 20) r_0^2$ based on the weighted average of $\Delta\sigma_{RS}(E_0 = 1.5 \text{ MeV})$ and $\Delta\sigma_{RS}(E_0 = 2.0 \text{ MeV})$. Note that our theoretical

TABLE I. Experimental relative intensity ratios.^a

E_0 (MeV)	Relative intensity
1.5	$Y_{RS}/Y_{KL}^1 \text{ RER} = 0.0477 \pm 0.0034$ (30%) ^b
	$Y_{KL}^1 \text{ RER}/Y_{K\alpha L}^1 = 0.0016 \pm 0.0004$ (25%) ^c
	$Y_{K\alpha L}^1/Y_{K\alpha_{1,2}} = 0.157 \pm 0.011$ (7%)
2.0	$Y_{RS}/Y_{K\alpha_{1,2}} = (1.20 \pm 0.58) \times 10^{-5}$ (48%)
	$Y_{RS}/Y_{KL}^1 \text{ RER} = 0.0684 \pm 0.0056$ (30%) ^b
	$Y_{KL}^1 \text{ RER}/Y_{K\alpha L}^1 = 0.0016 \pm 0.0004$ (25%) ^c
	$Y_{K\alpha L}^1/Y_{K\alpha_{1,2}} = 0.130 \pm 0.013$ (10%)
	$Y_{RS}/Y_{K\alpha_{1,2}} = (1.42 \pm 0.70) \times 10^{-5}$ (49%)

^a All intensities were measured using an EDdT crystal with the spectrometer in the \parallel mode.

^b Estimated reproducibility error. Statistical errors for these quantities are 7%–8%.

^c Jamison *et al.*, from Ref. 2.

TABLE II. IRRS cross sections in r_0^2 .

E_0 (MeV)	$\Delta\sigma_{RS}(\text{expt})^a$	$\sigma_{RS}(\text{est})^b$
1.5	4.2 ± 2.0	55 ± 27
2.0	4.6 ± 2.3	61 ± 30
	avg. ^c $= 4.4 \pm 1.5$	avg. ^c $= 58 \pm 20$
Theory ^d	3.88	50.8 61 ^e

^a Partial cross section for scattering into $1634 \leq E_f \leq 1640.5$ eV.

^b Estimate of total scattering cross section based on $\Delta\sigma_{RS}(\text{expt})$ in the manner of Sec. V.

^c Weighted average of 1.5- and 2.0-MeV data.

^d Based on integration over the appropriate range of

E_f .

^e Tulkki and Åberg in Ref. 14.

calculations in this paper include only the resonant contribution to the total scattering cross section whereas our experimental cross sections include both resonant and nonresonant contributions. A theoretical estimate by Tulkki and Åberg¹⁴ with the nonresonant part included yields $\sigma_{RS} = 61r_0^2$. The difference between these two estimates is due not only to the nonresonant part but also to the differences in the calculation of the $K\alpha$ emission probability and K absorption cross section. Cross-section values are tabulated in Table II.

VI. CONCLUSION

We have presented an experimental study of the internal resonance Raman scattering process in ion-induced Si K x-ray spectra obtained from thick targets. Our identification of the IRRS structure is based on both its predicted spectral shape and edge energy. We are able to measure a partial scattering cross section associated with this process which is in reasonable agreement with theoretical calculations. From this partial cross section we are able to estimate a value for the total scattering cross section into all angles and all allowed energies.

We have restricted our experiment to incident proton beams in order to minimize background radiation in the IRRS region. The use of proton beams also has the effect of minimizing the amount of L -shell ionization in the target. This increases the normal $K\alpha$ yield relative to the $K\alpha$ satellites and hence also the IRRS intensity. We have also restricted our study of the IRRS process to a single target element, Si. This was done in view of the difficulty of obtaining pure solid targets capable of withstanding high beam currents in the immediate range above $Z = 14$. Additionally, Utrianen¹⁹ has estimated that the IRRS cross

section drops off with increasing target Z .

Analyzing ion-induced x-ray spectra should not be thought of as an optimal method for investigating the IRRS process due to the nearby structures. Electron and x-ray induced spectra are capable of providing both higher count rates and lower background in the IRRS region. The significance of our observation of the IRRS process in ion-induced x-ray spectra rests upon two points: (i) it establishes, as has been noted here and in other work,^{3,4} a distinct, observable difference between processes which are internal to the atom (RA, RER) and those which are external to the atom (IRRS), and (ii) it establishes the fact that, although features from the internal atomic x-ray processes dominate, inelastic photon scattering processes are observable phenomena in thick-target x-ray spectra.

ACKNOWLEDGMENTS

We thank J. Utrianen and O. Keski-Rahkonen for making available their unpublished results. This work was supported in part by the Division of Chemical Sciences, U. S. Department of Energy.

APPENDIX: THICK-TARGET ANALYSIS

In this section we give the details of the target analysis required in order to extract IRRS yields and cross sections from ion bombardment of a thick solid target. A similar analysis for photon impact has been made previously by Keski-Rahkonen.²⁰ The incident ions producing the characteristic $K\alpha$ photons will be treated as a parallel beam of arbitrary cross section. The intensity of the beam is described by the number I_0 of monoenergetic ions, energy E , per unit time which pass through a unit area normal to the beam direction. The incident beam makes an angle α with the normal to the target surface as shown in Fig. 5. Neglecting losses due to straggling and small angle scattering, the rate of ions impinging on a differential element of surface area dA' located parallel to the surface is approximately independent of depth up to the ion range and is given by $I_0 dA' \cos\alpha$. The rate of $K\alpha$ photon production within a volume element $dV' = (dA' \cos\alpha) ds' = dA' dt'$ at a target depth t' (see Fig. 5) is given by $I_0 dV' n \sigma_{KX}(s')$, where n is the target atomic density and $\sigma_{KX}(s')$ is the K x-ray production cross section at an ion energy $E(s')$ where $s' = t'/\cos\alpha$ is the ion penetration depth.

The intensity of these $K\alpha$ photons on the surface of an imaginary sphere of radius r centered at dV' may be written

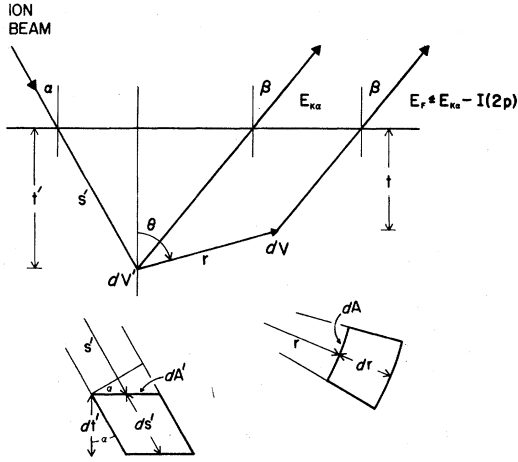


FIG. 5. Single and double scattering geometries for a thick solid target.

$$I' \equiv I_0 dV' n \sigma_{KX}(s') \exp(-\mu_2 r) / 4\pi r^2, \quad (19)$$

where $\mu_2 = \mu_2(E_{K\alpha})$ is the linear absorption coefficient for $K\alpha$ radiation. Using this we calculate the rate at which photons from dV' enter the spherical volume element dV (see Fig. 5) and are scattered into an energy interval $(E_f, E_f + \Delta E_f)$ via the resonant Raman process to be $I' dV n \Delta\sigma_{RS}(E_{K\alpha}; E_f)$. The quantity $\Delta\sigma_{RS}(E_{K\alpha}; E_f)$ refers to a differential segment of σ_{RS} responsible for scattering incident radiation ($E_i = E_{K\alpha}$) into the interval $(E_f, E_f + \Delta E_f)$. The rate at which Raman scattered photons in the energy interval ΔE_f from element dV reach the detector is given by

$$\begin{aligned} & I' dV n \Delta\sigma_{RS} \exp\left(\frac{-\mu_3 t'}{\cos\beta}\right) \left(\frac{d\Omega_B}{4\pi}\right) \\ &= I_0 \frac{dV'}{4\pi} \frac{dV}{r^2} n^2 \\ & \quad \times \sigma_{KX}(s') \Delta\sigma_{RS} \left(\frac{d\Omega_B}{4\pi}\right) \exp\left(-\mu_2 r - \frac{\mu_3 t'}{\cos\beta}\right), \quad (20) \end{aligned}$$

where $d\Omega_B$ is the solid angle subtended at dV by the detector (or spectrometer image slit) and $\mu_3 = \mu_3(E_f)$ is the linear absorption coefficient for the scattered radiation. Based on the theoretical development of Sec. III we have assumed that the scattered radiation is emitted isotropically from dV .

Integration of Eq. (20) over the sample volume dV (with origin at dV') gives the total detectable Raman yield within ΔE_f due to $K\alpha$ radiation from dV' . For a distant detector (or spectrometer image slit) we assume that the solid angle factor $d\Omega_B/4\pi$ is approximately constant (to within $\sim 1\%$) and that it may be moved outside of the integral to yield

$$\begin{aligned} Y_{RS}(dV'; E_f) & \equiv I_0 \frac{dV'}{4\pi} n^2 \sigma_{KX}(s') \Delta\sigma_{RS} \left(\frac{d\Omega_B}{4\pi}\right) \\ & \quad \times \int_V \exp\left(-\mu_2 r - \frac{\mu_3 t'}{\cos\beta}\right) \sin\theta d\phi dr. \quad (21) \end{aligned}$$

Equation (21) can be integrated over ϕ and also over the range of the ion beam to obtain the total detectable Raman yield within ΔE_f due to $K\alpha$ radiation from a column of differential cross section $dA' \cos\alpha$ along the beam path

$$\begin{aligned} Y_{RS}(\alpha, \beta; E_f) &= I_0 \frac{dA'}{2} n^2 \Delta\sigma_{RS} \left(\frac{d\Omega_B}{4\pi}\right) \cos\alpha \int_0^{\text{Range}} \sigma_{KX}(s') \exp\left(\frac{-\mu_3 t'}{\cos\beta}\right) \\ & \quad \times \left\{ \int_0^{t'} \int_{-1}^1 \left(\exp\left(\frac{\mu_3 r \cos\theta}{\cos\beta} - \mu_2 r\right) d(\cos\theta) dr \right. \right. \\ & \quad \left. \left. + \int_{t'}^{\infty} \int_{-1}^{\frac{t'}{r}} \exp\left(\frac{\mu_3 r \cos\theta}{\cos\beta} - \mu_2 r\right) d(\cos\theta) dr \right\} ds'. \quad (22) \end{aligned}$$

The integral in this expression may be evaluated numerically.

The next step involves the determination of the $K\alpha$ x-ray yield from the differential column discussed above. The detectable $K\alpha$ photon yield

from the volume element dV' is given by $I_0 dV' n \sigma_{KX}(s') (d\Omega_B/4\pi) \exp(-\mu_2 t'/\cos\beta)$. The total detectable yield from the column may now be found by integration along the beam path

$$Y_{K\alpha}(\alpha, \beta) \equiv I_0 dA' n \cos\alpha \left(\frac{d\Omega_B}{4\pi}\right) \int_0^{\text{Range}} \sigma_{KX}(s') \exp\left(\frac{-\mu_2 t'}{\cos\beta}\right) ds'. \quad (23)$$

This expression must also be evaluated numerically due to the lack of a simple algebraic form for $\sigma_{K\alpha}(s')$.

The ratio of $Y_{RS}(\alpha, \beta; E_f)$ to $Y_{K\alpha}(\alpha, \beta)$ now provides a measure of the relative yield of IRRS within ΔE_f to $K\alpha$ radiation for a given α and β due to a single differential column along the beam path

$$\frac{Y_{RS}(\alpha, \beta; E_f)}{Y_{K\alpha}(\alpha, \beta)} = \frac{\Delta\sigma_{RS}}{\sigma_{K\alpha}(0)} F(\alpha, \beta, E_0, E_f), \quad (24)$$

where $F(\alpha, \beta, E_0, E_f)$ is a dimensionless form factor including a factor $\sigma_{K\alpha}(0)$. Since all differential columns along the beam path are assumed to be identical in this model, Eq. (24) also represents the total measured relative yield of IRRS within ΔE_f to $K\alpha$ radiation. If the relative yield $Y_{RS}(\alpha, \beta; E_f)$ to $Y_{K\alpha}(\alpha, \beta)$ can be measured, then Eq. (24) may be used to estimate the cross section $\Delta\sigma_{RS}$.

As a simple cross check of the above derivation (independent of the assumptions made therein) we may evaluate the gross x-ray yields in terms of "escape efficiencies" for the Raman scattered and characteristic radiation. The measurable characteristic x-ray yield is given by $Y_{K\alpha}^{meas} = \epsilon_{K\alpha} Y_{K\alpha}^{total}$ where $\epsilon_{K\alpha} \leq 0.5$ is the escape efficiency of the characteristic target $K\alpha$ x-rays. Likewise, the measurable Raman scattered yield is $Y_{RS}^{meas}(E_f) = \epsilon_{RS} Y_{RS}^{total}(E_f)$ where $\epsilon_{RS} \leq 0.5$ is the escape efficiency of the Raman scattered radiation. $Y_{RS}^{total}(E_f)$ is given by

$$Y_{RS}^{total}(E_f) = (1 - \epsilon_{K\alpha}) \frac{\Delta\sigma_{RS}}{\sigma_{ABS}} Y_{K\alpha}^{total} \quad (25)$$

where $1 - \epsilon_{K\alpha}$ represents the fraction of the total characteristic radiation which is absorbed in the solid and $\Delta\sigma_{RS}/\sigma_{ABS}$ is the fraction of the absorbed radiation which scatters into $(E_f, E_f + \Delta E_f)$ via the resonant Raman process. Thus we have

$$\begin{aligned} Y_{RS}^{meas}(E_f) &= \epsilon_{RS} (1 - \epsilon_{K\alpha}) \frac{\Delta\sigma_{RS}}{\sigma_{ABS}} Y_{K\alpha}^{total} \\ &= \frac{\epsilon_{RS}}{\epsilon_{K\alpha}} (1 - \epsilon_{K\alpha}) \frac{\Delta\sigma_{RS}}{\sigma_{ABS}} Y_{K\alpha}^{meas}. \end{aligned} \quad (26)$$

Taking the ratio of $Y_{RS}^{meas}(E_f)$ to $Y_{K\alpha}^{meas}$ we obtain

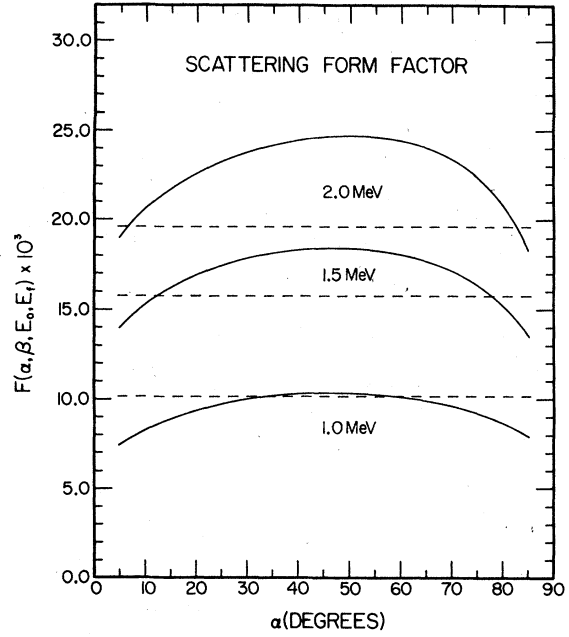


FIG. 6. $F(\alpha, \beta, E_0, E_f)$ vs α for the special case of $\beta = \frac{1}{2}\pi - \alpha$ and $E_f \approx E_f(\max)$. The solid lines represent the detailed evaluation of Eqs. (22) and (23). The dashed lines are based upon Eq. (28) using $\epsilon_{RS}, \epsilon_{K\alpha} = 0.5$.

$$\frac{Y_{RS}^{meas}(E_f)}{Y_{K\alpha}^{meas}} = \frac{\epsilon_{RS}}{\epsilon_{K\alpha}} (1 - \epsilon_{K\alpha}) \frac{\Delta\sigma_{RS}}{\sigma_{ABS}} = \frac{\Delta\sigma_{RS}}{\sigma_{K\alpha}(0)} F(E_0), \quad (27)$$

where E_0 is the incident ion energy and

$$F(E_0) = \frac{\epsilon_{RS}}{\epsilon_{K\alpha}} (1 - \epsilon_{K\alpha}) \frac{\sigma_{K\alpha}(0)}{\sigma_{ABS}(E_{K\alpha})}. \quad (28)$$

The results of the detailed calculation of $F(\alpha, \beta, E_0, E_f)$ for the special case of our experiment [$\beta = \frac{1}{2}\pi - \alpha, E_f \approx E_f(\max)$] are shown in Fig. 6. The results of the simple model given above assuming $\epsilon_{K\alpha}, \epsilon_{RS} = 0.5$ are seen to be in good agreement with the detailed calculation for $\alpha = 45^\circ$ and $E_0 = 1.0$ MeV. At higher energies the simple model begins to deviate from the detailed calculation for $\alpha = 45^\circ$. This is presumably due to the larger penetration of the projectile into the target and the resultant deviation of ϵ from the value of 0.5. The ϵ of 0.5 corresponds to one-half of the photons going into the target material and one-half being emitted outside of the target material. This assumption should be valid for isotropic radiation emitted very near the target surface.

¹P. Richard, J. Oltjen, K. A. Jamison, R. L. Kauffman, C. W. Woods, and J. M. Hall, Phys. Lett. **A54**, 169 (1975).

²K. A. Jamison, J. M. Hall, J. Oltjen, C. W. Woods,

Robert L. Kauffman, Tom J. Gray, and Patrick Richard, Phys. Rev. A **14**, 937 (1976).

³T. Åberg and J. Utriainen, Phys. Rev. Lett. **22**, 1346 (1969).

- ⁴T. Åberg and J. Utraiainen, *J. Phys. (Paris) C* **4**, 295 (1971).
- ⁵K. A. Jamison, J. M. Hall, and Patrick Richard, *J. Phys. B* **8**, L458 (1975).
- ⁶M. Sawada, K. Taniguchi, and H. Nakamura, *J. Phys. Soc. Jpn.* **33**, 1496 (1972).
- ⁷C. J. Sparks, Jr., *Phys. Rev. Lett.* **33**, 262 (1974).
- ⁸Y. B. Bannett, J. I. Gersten, N. Tzoar, and I. Freund, *Phys. Rev. Lett.* **36**, 882 (1976).
- ⁹Y. B. Bannett, D. C. Rapaport, and I. Freund, *Phys. Rev. A* **16**, 2011 (1977).
- ¹⁰P. Suortfi, Rep. Ser. Phys. Univ. Helsinki No. HV-P-139 (1977).
- ¹¹P. Eisenberger, P. M. Platzman, and H. Winick, *Phys. Rev. B* **13**, 2377 (1976).
- ¹²P. Eisenberger, P. M. Platzman, and H. Winick, *Phys. Rev. Lett.* **36**, 623 (1976).
- ¹³Y. B. Bannett and I. Freund, *Phys. Rev. Lett.* **34**, 372 (1975).
- ¹⁴J. Tulkki and T. Åberg, in *Abstracts of the Sixth International Conference on Atomic Physics*, edited by E. Anderson, E. Kravliya, and R. Peyerkop (Riga, USSR, 1978), p. 393.
- ¹⁵P. Nozières and E. Abrahams, *Phys. Rev. B* **10**, 3099 (1974).
- ¹⁶K. A. Jamison, Ph.D. thesis (Kansas State University, 1978) (unpublished).
- ¹⁷E. Merzbacher and W. H. Lewis, *Handbuch der Physik* (Springer-Verlag, Berlin, 1958), Vol. 34, p. 166.
- ¹⁸J. H. Scofield, LLL Report No. UCRL-51326, 1973 (unpublished).
- ¹⁹J. Utraiainen (private communication).
- ²⁰O. Keski-Rahkonen (private communication).